photonics

MDPI

Article

A Multiscale Computational Framework for Tolerance and Sensitivity Analysis of Manufacturing and Alignment Errors in Freeform Optical Surfaces

Reem Al Salamah *, Norah Alqahtani, Abeer Al-Modlej and Ghadah Hamad Alsowygh

Department of Physics and Astronomy, College of Science, King Saud University, Riyadh 11451, Saudi Arabia; 444200655@student.ksu.edu.sa (N.A.); amodlej@ksu.edu.sa (A.A.-M.); galsowygh@ksu.edu.sa (G.H.A.)
* Correspondence: ralsalamah1@ksu.edu.sa

Abstract

Freeform optical surfaces offer additional freedom for aberration control, but their performance is highly sensitive to manufacturing and alignment errors that occur simultaneously and across several spatial scales. This paper presents a general computational framework for the tolerance and sensitivity analysis of freeform surfaces. The framework superimposes low-order Zernike form error, mid-spatial-frequency ripple, high-spatial-frequency roughness, tilt, and axial positioning error on a single sampled surface; propagates the resulting wavefront through a scalar Fourier-optics model to obtain the PSF, MTF, RMS wavefront error, and Strehl ratio; and combines Monte Carlo simulation, variance-based (Sobol) global sensitivity analysis, and yield-based tolerance allocation. It requires only the wavelength, aperture, nominal surface sag, and the statistical tolerance of each error source, and its numerical implementation is verified against analytic solutions. An F/2 freeform singlet is used as a demonstration. The analysis shows that error sources acting on the same wavefront mode, here surface defocus and axial position, interact rather than add. Consequently, one-at-a-time evaluation and conventional root-sum-square budgets misestimate the Strehl ratio, although they remain adequate for the RMS wavefront error, and a Strehl-based, yield-driven allocation meets the performance target at substantially lower tolerance cost than uniform tightening.

Keywords: freeform optics; Zernike polynomials; tolerance analysis; PSF; MTF; Monte Carlo simulation; sensitivity coefficient; alignment errors; mid-spatial-frequency errors

1. Introduction

Freeform optical surfaces offer high flexibility in controlling aberrations and have enabled compact, high-performance imaging, illumination, and augmented-reality systems [1,2]. However, this performance is highly sensitive to manufacturing and alignment errors, which distort the wavefront and degrade image quality [3]. Tolerance analysis of optical systems has traditionally relied on the sensitivity and Monte Carlo tools of commercial design software, in which each surface is assigned global RMS or peak-to-valley limits and the effects of the individual perturbations are combined by linear sensitivities and root-sum-square (RSS) rules [4,5]. For freeform surfaces, which have no rotational symmetry and are usually produced by sub-aperture machining, these global criteria are increasingly recognized as insufficient, and several new approaches have been reported. **Figure 1 illustrates ray propagation through an ideal freeform lens and shows howmanufacturing and alignment errors alter the ray paths.**

Check for updates

Received: 9 September 2026
Revised: 15 November 2026
Accepted: 20 November 2026
Published: 28 November 2026

Copyright: © 2026 by the authors. Licensee MDPI, Basel, Switzerland. This article is an open access article distributed under the terms and conditions of the Creative Commons Attribution (CC BY) license.

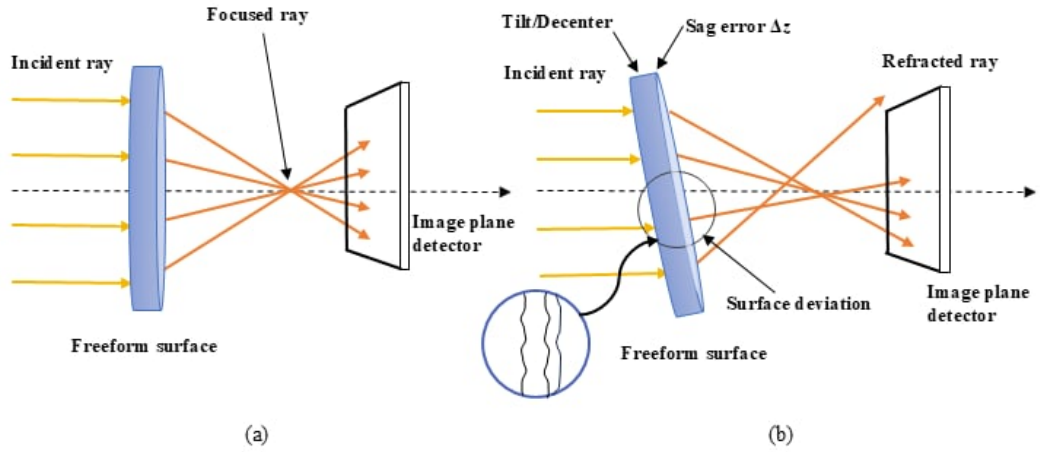

Figure 1. (**a**) Ideal freeform lens focusing collimated rays to a single point. (**b**) Freeform lens with manufacturing and alignment errors that deflect rays and introduce wavefront aberrations. **The arrows indicate the direction of light propagation before and after refraction by the freeform lens.**

Deng et al. introduced local tolerances that assign a different allowable deviation to each region of an optical surface and used them to evaluate surface quality [6]. Fan et al. extended this idea to surface frequency bands, deriving the allowable surface variation in each band for a prescribed wavefront error [7], and later used critical-ray aiming and iterative critical ray tracing to compute local tolerances of freeform imaging systems efficiently [8]. Chen et al. moved the evaluation criterion from the optical image to the final output of optical–digital imaging systems, in which image-processing algorithms partly compensate for the optical errors [9]. Other studies have addressed freeform metrology, including surface registration and fitting [10] and on-machine measurement with dynamic error calibration [11].

These methods have substantially improved how tolerances are specified for freeform surfaces, but they share three limitations that motivate the present work. First, most treat one class of error at a time, either surface-form deviations within given frequency bands or measurement errors, and do not apply low-order form error, MSF ripple, HSF roughness, and alignment errors simultaneously to the same surface. Second, the derived tolerances are mostly deterministic limits; the statistical yield of a batch of parts with random errors is not evaluated. Third, sensitivity is assessed locally (by linear sensitivities or for one perturbation at a time), so interactions between error sources, which can dominate when two errors act on the same wavefront mode, are not quantified. Table 1 summarizes representative methods and these differences. Zernike representation, Fourier-optics image evaluation, Monte Carlo tolerancing and spatial-frequency error classification are each well established. The contribution of this work lies not in these individual tools but in what their joint, verified treatment reveals that separate analyses cannot. Specifically, this work provides: (1) a unified error model in which low-order form error, MSF ripple, HSF roughness, tilt and axial positioning error act simultaneously on one surface, verified against analytic solutions; (2) a variance-based (Sobol) sensitivity analysis that identifies the dominant error sources and their interactions, which a linear sensitivity analysis of the same data fails to capture; (3) a demonstration that error sources acting on the same wavefront mode do not combine additively or multiplicatively; (4) evidence that the conventional RSS estimate, adequate for the RMS wavefront error, fails for the Strehl ratio; and (5) a yield-based tolerance allocation and compensator analysis that convert these results into design decisions. The framework is demonstrated on an F/2 freeform singlet.

Table 1. Comparison of representative manufacturing-error analysis methods reported in the literature with the proposed methodology.

Reference	Simultaneous + Alignment Errors	Method	Global Sensitivity/ Yield-Based Allocation	Limitation
Deng et al. (2022)	Local surface tolerance and quality evaluation	No (surface form only)	No	Deterministic local limits; no statistical yield or alignment errors [6].
Duan & Zhang (2023)	No	Surface registration and fitting for freeform metrology.	No	Focused on metrology; no Monte Carlo tolerance or sensitivity analysis [10].
Fan et al. (2024)	Partly (frequency bands; no alignment errors).	Surface-frequency-band tolerance analysis.	No	Focused on wavefront/surface variation; does not provide a unified manufacturing-error simulation framework [7].
Wang et al. (2025)	No	Dynamic error calibration for on-machine metrology.	No	Focused on measurement and calibration rather than optical performance prediction or tolerance sensitivity [11].
Chen et al. (2026)	No	Image-quality-based tolerancing of optical–digital systems.	No	Criterion on the restored image; no multiscale surface-error model [9].
This work	yes	Multiscale surface model (Zernike low-order form + sinusoidal MSF + filtered random HSF + rigid-body alignment) + Fourier optics + Monte Carlo + Sobol analysis.		Comprehensive analysis of low- and high-order manufacturing errors with integrated sensitivity analysis.

2. Methodology

2.1. Optical System and Surface Representation

The framework is demonstrated on a plano-convex singlet (D = 25 mm, f = 50 mm, F/2) used on-axis with an object at infinity at λ = 550 nm, with the aperture stop at the lens (Table 2). Its curved surface, a base sphere of radius Rc = f(n − 1) = 25 mm, carries a small non-rotationally symmetric departure and all manufacturing errors; the plane rear surface is assumed perfect, and the lens is treated as a thin, non-dispersive element (n = 1.50) [12]. This simple configuration allows the numerical results to be checked against analytic solutions (Section 2.4) and the effect of each error source to be isolated. Unless otherwise stated, the parameters in Table 2 were kept fixed in all simulations.

Unless otherwise stated, the parameters in Table 2 were kept fixed in all simulations.

The surface sag is represented using Zernike polynomials [13,14]:

Other bases, such as XY and Forbes Q-polynomials, can also describe freeform surfaces [13,14]; Zernike polynomials are used here because they are orthogonal over the circular pupil and map directly to wavefront aberrations. Zernike polynomials were adopted because (i) they are orthogonal over the circular aperture, so the coefficients can be sampled independently and their RMS contributions add in quadrature; (ii) low-order form errors are routinely measured and specified as Zernike coefficients, so the error statistics can be taken directly from metrology; and (iii) each term corresponds to a classical aberration, which allows physical interpretation of the results, such as the defocus–axial interaction (Section 3.9). (iv) Because all optical metrics are computed from the sampled surface (Section 2.4), the basis does not affect the evaluation, and any other representation or a

measured sag map can replace Equation (3); a Q-polynomial or Chebyshev basis would be preferable for large departures or non-circular apertures.

Table 2. Parameters employed throughout the simulations.

Parameters	Value
Wavelength λ	550 nm
Aperture radius a	12.5 mm
Aperture diameter D	25 mm
Focal length f	50 mm
Computational grid N	256 × 256 pixels
Refractive index n	1.50
F-number N	2.0
Diffraction cutoff frequency	909.09 cycles/mm
Computational window	50 mm (2D, two-fold zero padding)
system	Plano-convex singlet, object at infinity.
Field	On-axis
Aperture stop	At the lens
Base surface	Sphere, Rc = 25 mm (plane rear surface).
Approximation	Thin lens, monochromatic

A sphere is rotationally symmetric, so its departure from the base sphere contains only the m = 0 terms (defocus- and spherical-like terms). The nominal surface considered here also contains astigmatism and coma terms (m = ±2, ±1), which cannot be produced by any aspheric surface; this non-rotationally symmetric departure is what defines the surface as freeform. Such departures are used in off-axis, tilted, or non-symmetric systems to correct field-dependent astigmatism and coma. hey are usually produced by sub-aperture machining and polishing, which leaves directional mid-spatial-frequency ripple (modeled here with an orientation of 25°), and because their lack of symmetry makes alignment errors harder to compensate. An aspheric surface is a special case of the model, obtained by setting the m ≠ 0 coefficients to zero, so the framework applies to a sphere as well.

2.2. Propagation of Surface Perturbations to Optical Performance

The nominal optical surface is a plano-convex base sphere of radius Rc = f(n − 1) = 25 mm. The freeform character of the manufactured surface is introduced by a non-rotationally symmetric Zernike departure, expanded over the normalized circular aperture as:

$$Z_0(\boldsymbol{\rho}, \boldsymbol{\theta}) = \sum_{j=1}^{J} \boldsymbol{a_j Z_j}(\boldsymbol{\rho}, \boldsymbol{\theta}), \tag{1}$$

where $\mathbf{Z_0}$ is the nominal surface sag. $\boldsymbol{a_j}$ is the coefficient associated with the j-th Zernike mode, $\boldsymbol{Z_j}$ is the corresponding Zernike polynomial, and J is the total number of modes included in the surface representation. The normalized radial coordinate is defined by $\boldsymbol{\rho} = \frac{r}{R}$, where R is the pupil radius and $\mathbf{0} \leq \boldsymbol{\rho} \leq \mathbf{1}$. Manufacturing and alignment imperfections introduce a surface perturbation $\boldsymbol{\Delta z}(\boldsymbol{\rho}, \boldsymbol{\theta}; \mathbf{p})$, where:

$$\mathbf{P} = [\boldsymbol{P_1}, \boldsymbol{P_2}, \ldots, \boldsymbol{P_k}]^{\mathbf{T}}, \tag{2}$$

P is the vector of error parameters. In the present model, p contains the amplitudes of defocus, spherical aberration, mid-spatial-frequency ripple, surface roughness, tilt, and axial positioning error. The manufactured surface is therefore written as:

$$\boldsymbol{Z_m}(\boldsymbol{\rho}, \boldsymbol{\theta}; \mathbf{P}) = \boldsymbol{Z^0}(\boldsymbol{\rho}, \boldsymbol{\theta}) + \boldsymbol{\Delta Z}(\boldsymbol{\rho}, \boldsymbol{\theta}; \mathbf{P}), \tag{3}$$

The perturbation can be decomposed into deterministic and stochastic components:

$$\boldsymbol{\Delta Z} = \boldsymbol{\Delta Z}_{\mathbf{form}} + \boldsymbol{\Delta Z}_{\mathbf{MSF}} + \boldsymbol{\Delta Z}_{\mathbf{rough}} + \boldsymbol{\Delta Z}_{\mathbf{align}}, \tag{4}$$

where ΔZ_{form}, represents low-order form error, $\Delta Z_{MSF,}$ represents mid-spatial-frequency ripple, ΔZ_{rough}, represents high-spatial-frequency surface roughness, and ΔZ_{align}, describes alignment-induced perturbations. For a transmissive optical surface with refractive index n, the first-order optical path difference produced by the surface perturbation is approximated by

$$W(\boldsymbol{\rho}, \boldsymbol{\theta}; \mathbf{P}) = (n - 1)\, \boldsymbol{\Delta Z}(\boldsymbol{\rho}, \boldsymbol{\theta}; \mathbf{P}), \tag{5}$$

Here, W denotes the wavefront or OPD perturbation relative to the nominal surface. This expression assumes small surface slopes, near-normal incidence, scalar propagation, and a homogeneous surrounding medium. The piston term does not influence image formation and is therefore removed by subtracting the pupil-averaged OPD as follows:

$$\tilde{W}(\boldsymbol{\rho}, \boldsymbol{\theta}; \mathbf{P}) = W(\boldsymbol{\rho}, \boldsymbol{\theta}; \mathbf{P}) - \langle W(\boldsymbol{\rho}, \boldsymbol{\theta}; \mathbf{P}) \rangle_A, \tag{6}$$

where $\langle W(\boldsymbol{\rho}, \boldsymbol{\theta}; P) \rangle_{\mathrm{A}}$ denotes the average over the illuminated pupil area A. In the present tolerance analysis, we retain these terms whenever they represent physical manufacturing or alignment errors under investigation. The corresponding phase perturbation is

$$\boldsymbol{\phi}(\boldsymbol{\rho}, \boldsymbol{\theta}; \mathbf{P}) = \frac{2\boldsymbol{\pi}}{\boldsymbol{\lambda}} \tilde{W}(\boldsymbol{\rho}, \boldsymbol{\theta}; \mathbf{P}), \tag{7}$$

where λ is the operating wavelength; thus, a perturbation in the Zernike coefficient propagates linearly into OPD and phase. We compute the complex pupil function, PSF, OTF, and MTF in the standard way [15]; we normalize the PSF by its total energy, not its peak, so the Strehl ratio is preserved. The modulation transfer function is

$$\mathbf{MTF}\left(f_x, f_y; \mathbf{P}\right) = \frac{\left|\mathbf{OTF}\left(f_x, f_y; \mathbf{P}\right)\right|}{\left|\mathbf{OTF}(\mathbf{0}, \mathbf{0}; \mathbf{P})\right|}, \tag{8}$$

Therefore, manufacturing-induced phase errors modify the complex pupil, redistribute energy in the PSF, and reduce the contrast transfer at nonzero spatial frequencies. The RMS wavefront error over the pupil is calculated as

$$\boldsymbol{\sigma}_W(\mathbf{P}) = \sqrt{\left\langle \tilde{W}^2(\boldsymbol{\rho}, \boldsymbol{\theta}; \mathbf{P}) \right\rangle_A}, \tag{9}$$

The Strehl ratio is calculated directly from the ratio of the aberrated and diffraction-limited PSF peak intensities:

$$S_{\mathbf{PSF}}(\mathbf{P}) = \frac{\max\limits_{u,v}\left[\mathbf{PSF}_{\mathbf{N,ab}}(u, v; \mathbf{P})\right]}{\max\limits_{u,v}\left[\mathbf{PSF}_{\mathbf{N,dl}}(u, v)\right]}, \tag{10}$$

The diffraction-limited and aberrated PSFs in Equation (10) must be generated using the same sampling grid, pupil amplitude, propagation scaling, and total-energy normalization. The complete propagation chain is summarized as

$$\boldsymbol{\Delta Z} \rightarrow W \rightarrow \boldsymbol{\phi} \rightarrow \mathfrak{D} \rightarrow \mathbf{PSF} \rightarrow \mathbf{MTF}, \ \{\boldsymbol{\sigma}_W, S\} \rightarrow S_{M,P_k}, \tag{11}$$

This formulation establishes a direct relationship between the physical surface perturbations and the resulting degradation of the optical performance. The Zernike expansion in is used only for the nominal freeform departure and the low-order form errors [7]. The MSF ripple, HSF roughness, and alignment errors are generated in their own physical representations (Sections 2.3 and 2.5) and superimposed on a common Cartesian grid (Equation (4)), and the optical metrics are computed from this sampled wavefront without any modal fit. The axial positioning error produces the same r^2 wavefront as Zernike defocus, which is the physical origin of the interaction reported in Section 3.9.

2.3. Modeling of Manufacturing Errors

Limitations in machining accuracy, finishing, and tool-path generation cause deviations from the nominal freeform shape across spatial scales. Following the standard spatial-frequency decomposition used in fabrication and metrology, these deviations are divided into low-order form errors, MSF ripple, and HSF roughness, each modeled independently before being combined.

2.3.1. Low-Order Form Errors

Low-order form errors are long-wavelength deviations of the global surface shape caused by polishing inaccuracies, tool calibration errors, and systematic machining deviations. They are represented by the six most common low-order Zernike terms (Table 3):

$$\boldsymbol{\Delta Z_{\text{form}}(\rho,\theta) = a_2^0 Z_2^0 + a_2^2 Z_2^2 + a_2^{-2} Z_2^{-2} + a_3^1 Z_3^1 + a_3^{-1} Z_3^{-1} + a_4^0 Z_4^0,} \quad (12)$$

where a_m^n are the Zernike coefficients (surface sag, in nm) and Z_m^n are the normalized Zernike polynomials defined over the unit pupil ($0 \le \rho \le 1$), listed in Table 3.

Table 3. Normalized Zernike polynomials used to represent the low-order form errors (Equation (28)) and the one-sigma tolerance assigned to each coefficient in the Monte Carlo analysis.

Term	Symbol	Polynomial Z_n^m(ρ, θ)	1σ Tolerance
Defocus	Z_2^0	$\sqrt{3}\,(2\rho^2 - 1)$	80 nm
Astigmatism 0°	Z_2^2	$\sqrt{6}\,\rho^2 \cos 2\theta$	40 nm
Astigmatism 45°	Z_2^{-2}	$\sqrt{6}\,\rho^2 \sin 2\theta$	30 nm
Coma X	Z_3^1	$\sqrt{8}\,(3\rho^3 - 2\rho) \cos\theta$	35 nm
Coma Y	Z_3^{-1}	$\sqrt{8}\,(3\rho^3 - 2\rho) \sin\theta$	20 nm
Spherical aberration	Z_4^0	$\sqrt{5}\,(6\rho^4 - 6\rho^2 + 1)$	50 nm

2.3.2. Mid-Spatial-Frequency Ripple

MSF ripple arises from periodic tool marks left by diamond turning, milling or sub-aperture polishing; it is not efficiently represented by low-order Zernike terms and is therefore modeled as a two-component sinusoid:

$$\boldsymbol{\Delta Z_{\text{MSF}}(x,y) = A_r\left[\sin\left(\frac{2\pi x'}{p} + \varphi\right) + 0.35\sin\left(\frac{2\pi y}{0.75\,p} + 0.7 + \varphi\right)\right], \quad x' = x\cos\theta_r + y\sin\theta_r,} \quad (13)$$

where A_r is the ripple amplitude, $\mathbf{p} = 1.5$ mm is the ripple period, $\boldsymbol{\theta_r} = 25°$ is the ripple orientation, and φ is a random phase offset. The second term is a weaker secondary ripple (35% amplitude, period 0.75p). In the Monte Carlo analysis. $\mathbf{A_r} \sim N(0, 40\text{ nm})$ and $\varphi \sim U[0, 2\pi)$. The period p = 1.5 mm (D/p ≈ 17) lies in the middle of the range typical of sub-aperture polishing; the sensitivity to p over 0.25–5 mm is examined on a 1024 × 1024 grid.

2.3.3. High-Spatial-Frequency Surface Roughness

HSF roughness consists of microscopic polishing residues that scatter light without changing the surface shape. Because it arises from many independent mechanisms, it is modeled as a band-limited Gaussian random field: a white-noise field n(x, y) is high-pass filtered, made zero-mean over the pupil and scaled to the RMS roughness $\boldsymbol{\sigma_r}$:

$$\boldsymbol{\Delta Z_{\text{rough}}(x,y) = \sigma_r \frac{\tilde{n}(x,y)}{\sqrt{\langle \tilde{n}^2 \rangle_A}}, \qquad \tilde{n} = \mathcal{F}^{-1}\{H(f)\,\mathcal{F}\{n\}\} - \left\langle \mathcal{F}^{-1}\{H(f)\,\mathcal{F}\{n\}\} \right\rangle_A,} \quad (14)$$

$$\boldsymbol{H(f) = 1 - exp\left[-\left(\frac{f}{f_c}\right)^4\right], \qquad f = \sqrt{f_x^2 + f_y^2}, \qquad f_c = \frac{1}{0.5\,mm},} \quad (15)$$

where $\langle\cdot\rangle_A$ is the pupil average and H(f) a super-Gaussian high-pass filter whose cutoff fc = 2 cycles/mm separates the roughness from the MSF band. A new noise field is generated in each realization, and $\boldsymbol{\sigma_r}$ is drawn from N(5 nm, 2 nm), folded to positive values. The three components are assumed statistically independent and are superimposed linearly (Equation (4)), which is valid because their amplitudes are small compared with the nominal sag.

2.4. Numerical Fourier-Optics Implementation

We evaluated the optical performance of the manufactured freeform surface using scalar Fourier optics under the Fraunhofer diffraction approximation. After constructing the manufactured surface by combining the nominal geometry with manufacturing and alignment perturbations, we computed the optical path difference (OPD) according to Equation (5). We removed the piston component from the wavefront before further processing to retain only wavefront distortions that affect image quality. The corresponding phase distribution was then calculated using Equation (7),

$$\boldsymbol{\phi}(x,y) = \frac{2\pi}{\lambda}\tilde{W}(x,y), P(x,y) = A(x,y)e^{i\boldsymbol{\phi}(x,y)}, \tag{16}$$

where $W(x,y)$ denotes the piston-removed optical path difference, and $\boldsymbol{\lambda}$ is the operating wavelength. The phase distribution was incorporated into the complex pupil function, where $A(x,y)$ represents the circular aperture function. We assumed uniform illumination across the pupil throughout the simulations. The complex optical field in the focal plane was obtained by applying a two-dimensional Fast Fourier Transform (FFT) to the complex pupil function. Before the Fourier transform, the pupil function was shifted to the center of the computational grid using the FFT-shift operation to ensure correct spatial-frequency mapping. The image-plane complex amplitude was therefore calculated as

$$U(u,v) = \mathfrak{F}\{\mathfrak{P}(x,y)\}, \mathbf{PSF}(u,v) = |U(u,v)|^2, \tag{17}$$

where $F\{\cdot\}$ denotes the two-dimensional Fourier transform. The point spread function (PSF) was subsequently obtained from the squared magnitude of the complex field.

As in Section 2.2, the PSF was normalized by its total energy rather than its peak, which preserves the definition of the Strehl ratio, and the OTF and MTF were computed from the normalized PSF using Equation (8). All numerical parameters (sampling, grid size, zero padding, wavelength, aperture and propagation distance) were identical for the nominal and perturbed systems, so that differences in the optical metrics arise only from the manufacturing and alignment errors, not from discretization.

We developed the numerical implementation in **MATLAB R2026b** using double-precision arithmetic. Two-dimensional FFT operations were performed using the built-in fft2 routine, while zero-frequency centering was achieved through the fftshift function. Random manufacturing errors were generated using MATLAB's Gaussian random-number generator for the roughness model and deterministic analytical expressions for the low-order form error and ripple components. This implementation provides a computationally efficient framework for large-scale Monte Carlo tolerance analysis while maintaining numerical stability and reproducibility.

2.5. Alignment Error Modeling

In addition to manufacturing-induced surface deviations, alignment errors introduced during assembly and integration significantly affect the optical performance of freeform systems. Even a surface manufactured within specification can be degraded by alignment errors introduced during assembly. The framework includes the two most common of these: tilt and axial positioning error.

2.5.1. Tilt Error

Tilt error, a small rotation of the element relative to the optical axis caused by assembly, mounting or thermal effects, produces an approximately linear wavefront tilt that deflects the transmitted rays. For small angles, the surface tilt is approximated by:

$$\boldsymbol{\theta} \ll \mathbf{1}, \boldsymbol{\Delta Z_{\text{tilt}}}(x, y) = x\tan\boldsymbol{\theta}_x + y\tan\boldsymbol{\theta}_y, \tag{18}$$

For small angles:

$$\tan\boldsymbol{\theta} \approx \boldsymbol{\theta}, \boldsymbol{\Delta Z_{\text{tilt}}}(x, y) \approx x\,\boldsymbol{\theta}_x + y\,\boldsymbol{\theta}_y, \tag{19}$$

The linear approximation is valid because the investigated alignment errors are significantly smaller than one degree. Because the tilts considered (tens of μrad) are far below one degree, higher-order terms are negligible.

2.5.2. Axial Positioning Error

An axial displacement $\boldsymbol{\delta z}$ of the lens, caused by spacer, mounting, or thermal errors, shifts the focal plane relative to the detector and produces a defocus wavefront, represented here by the equivalent surface term

$$\boldsymbol{\Delta Z_{\text{axial}}}(x, y) = \frac{\boldsymbol{\delta z}}{2f^2(n-1)}\left(x^2 + y^2\right), \tag{20}$$

where f is the focal length and n is the refractive index. After conversion to optical path difference with Equation (8), this term gives $W(r) = \delta z \cdot r^2/(2f^2)$, that is, a defocus coefficient $W_{020} = \delta z \cdot a^2/(2f^2) = \delta z/(8N^2)$ at the pupil edge r = a, where N = f/D is the F-number. For the present F/2 system, a displacement of 20 μm therefore produces $W_{020} = 0.625$ μm, more than one wavelength at 550 nm. This strong sensitivity of fast systems to axial position is examined in Section 3.

2.5.3. Combined Model

The complete manufactured optical surface is obtained by combining the manufacturing-induced surface perturbation with the alignment-induced errors. Assuming that manufacturing errors and alignment errors (tilt and axial position) are independent

$$\boldsymbol{\Delta Z_{\text{total}}} = \boldsymbol{\Delta Z_{\text{manufacturing}}} + \boldsymbol{\Delta Z_{\text{tilt}}} + \boldsymbol{\Delta Z_{\text{axial}}}, \tag{21}$$

$$\boldsymbol{Z_{final}} = \boldsymbol{Z^0} + \boldsymbol{\Delta Z_{form}} + \boldsymbol{\Delta Z_{MSF}} + \boldsymbol{\Delta Z_{rough}} + \boldsymbol{\Delta Z_{tilt}} + \boldsymbol{\Delta Z_{axial}}, \tag{22}$$

This perturbed surface serves as input to the Fourier-optics model in Section 2.4, which computes the OPD, PSF, MTF, RMS wavefront error, and Strehl ratio.

2.6. Monte Carlo and Analysis

Because the manufacturing and alignment errors are random, the performance is described statistically. In each realization, every error parameter is drawn independently as

$$\boldsymbol{P_i} \sim \mathcal{N}(\boldsymbol{\mu_i}, \boldsymbol{\sigma_i^2}), \tag{23}$$

where $\boldsymbol{P_i}$ is the *ith* manufacturing parameter, $\boldsymbol{\mu_i}$ is the nominal value, and $\boldsymbol{\sigma_i}$ is the manufacturing tolerance. With the means and one-sigma tolerances listed in Table 4, the MSF phase is uniform on $[0, 2\pi)$, and a new roughness field is generated (Section 2.3). The combined surface error (Equation (4)) is propagated with the Fourier-optics model of Section 2.4 to obtain the RMS wavefront error, PSF, MTF, and Strehl ratio. The analysis used 500 realizations on the 256 × 256 grid with a fixed random seed for reproducibility. Each metric is summarized by its mean, standard deviation, median, 5th and 95th percentiles, and the 95% confidence interval of the mean ($\mu \pm 1.96\sigma/\sqrt{N}$).

Table 4. Probability distributions and tolerance parameters used in the Monte Carlo analysis.

Parameter	Distribution	Mean	Standard Deviation
Defocus coefficient	Gaussian	0	80 nm
Astigmatism 0°	Gaussian	0	40 nm
Astigmatism 45°	Gaussian	0	30 nm
Coma X	Gaussian	0	35 nm
Coma y	Gaussian	0	20 nm
Spherical aberration	Gaussian	0	50 nm
MSF Ripple amplitude	Gaussian	0	40 nm
HSF roughness (RMS)	Gaussian	5 nm	2 nm
Axial positioning error	Gaussian	0	20 µm
x-tilt	Gaussian	0	30 µrad
y-tilt	Gaussian	0	20 µrad
Monte Carlo realizations	-	500	-
Random seed	Fixed	500	-

The one-sigma values in Table 4 represent precision freeform fabrication and assembly. The low-order form tolerances (20–80 nm, about $\lambda/27$–$\lambda/7$) correspond to a surface-figure specification of roughly $\lambda/4$–$\lambda/2$ peak-to-valley, typical of sub-aperture-polished freeform surfaces. The MSF amplitude (40 nm) lies in the range of residual tool-path ripple, the HSF roughness (5 ± 2 nm RMS) is conservative for polished or diamond-turned surfaces (1–5 nm RMS), and the alignment tolerances (20 µm axial, 20–30 µrad tilt) are representative of a precision lens cell. Because these values are assumptions rather than process data, their influence is quantified explicitly through the Sobol indices (Section 3.9) and the yield-based reallocation (Section 3.9).

2.7. Verification and Treatment of Tilt and Focus

The implementation was verified in two ways (Section 3.5). The computed Strehl ratio of pure defocus was compared with the exact value $S = [\sin(\pi W_{020}/\lambda)/(\pi W_{020}/\lambda)]^2$ for $W_{020}/\lambda = 0.05$–0.40, where $W_{020} = 2\sqrt{3}(n-1)a_2{}^0$, and sampling convergence was checked by repeating 20 realizations with an additional two-fold zero padding. Because tip/tilt only displaces the PSF but causes an artificial Strehl loss on a finite grid, the Strehl ratio is computed from the tip/tilt-removed wavefront, and the image displacement $f(n-1)\tan\theta$ is reported separately. To represent refocusing after assembly, a second Monte Carlo analysis also removes the best-fit r^2 term (focus compensator), whose coefficient gives the required refocus δz through Equation (10).

2.8. Sobol Analysis

The Strehl ratio and RMS wavefront error depend on the square of each zero-mean error; their local derivatives vanish, and a linear regression cannot represent them; global variance-based (Sobol) indices were therefore used. The first-order index S_i gives the fraction of the output variance due to parameter i alone, and the total index S_T_i includes its interactions; both were estimated with the Saltelli sampling scheme and the estimators of Saltelli et al. [16] and Jansen [17]:

$$S_i = \frac{\frac{1}{N}\sum_{j=1}^{N} f(\mathbf{B})_j\left[f\left(\mathbf{A}_{\mathbf{B}}^{(i)}\right)_j - f(\mathbf{A})_j\right]}{V(Y)}, S_{Ti} = \frac{\frac{1}{2N}\sum_{j=1}^{N}\left[f(\mathbf{A})_j - f\left(\mathbf{A}_{\mathbf{B}}^{(i)}\right)_j\right]^2}{V(Y)}, \quad (24)$$

where A and B are two independent N × k sample matrices drawn from the distributions in Table 4, $A,B^{(i)}$ equals A with its *ith* column taken from B, and V(Y) is the output variance. With N = 1000 and k = 11 parameters, N(k + 2) = 13,000 model evaluations were required. The 95% confidence intervals were obtained from 200 bootstrap resamples. The difference

$\Sigma S_{ti} - \Sigma S_i$ measures the part of the variance caused by interactions. Sobol indices are fractions of the output variance; they are dimensionless, non-negative, and independent of parameter units, so you can compare surface-form (nm), alignment (µm, µrad), and roughness parameters directly. Each index measures the share of the variance caused by a parameter's own tolerance (Table 4) and decreases if that tolerance is tightened. The indices carry no sign, because the Strehl ratio decreases for deviations of either sign. The indices were computed for the tip/tilt-removed Strehl ratio and for the RMS wavefront error both with the tilt retained and with tip/tilt removed.

2.9. RSS Estimate and Yield-Based Tolerance Allocation

The conventional root-sum-square (RSS) estimate evaluates each parameter alone at $\pm 1\sigma$ and combines the resulting changes ΔM_i in quadrature:

$$S_{RSS} = S_0 - \sqrt{\sum_i \Delta S_i^2}, \qquad RMS_{RSS} = \sqrt{RMS_0^2 + \sum_i \Delta\left(RMS^2\right)_i}, \tag{25}$$

where S_0 and RMS_0 refer to the nominal configuration. For tolerance allocation, each one-sigma tolerance is rescaled as $\sigma_i' = g \cdot w_i \cdot \sigma_i$. The weights $w_i = (c\bar{c}/c_i)^{1/2}$ equalize the contribution c_i of each parameter to the chosen metric (uniform, RMS-based or Strehl-based budget); they are limited to the range $[1/3, 3]$ and normalized to a geometric mean of one. The common scale g is found by bisection so that Strehl ≥ 0.80 is reached by 90% of 500 Monte Carlo realizations, and the result is validated on 1000 independent realizations. The tolerance cost is expressed by the index $C = \text{mean}(\sigma_i/\sigma_i')$, which equals 1 for the original tolerances and increases as tolerances are tightened.

2.10. Design Workflow for Low-Sensitivity Freeform Systems

Together, these analyses form a five-step design workflow: (1) define the nominal system and the statistical error model (Tables 2 and 4) and verify the numerical model (Section 3.1); (2) predict the yield, i.e., the fraction of parts with Strehl $\geq$ S_min, by Monte Carlo analysis; (3) identify the dominant parameters (large S_Ti) and interacting errors (large ΣS_Ti $-$ ΣS_i) from the Sobol indices; (4) add a compensator if a single alignment degree of freedom dominates, otherwise tighten the dominant parameters and relax the insensitive ones; and (5) solve the yield-based allocation problem

$$\min_{\boldsymbol{\sigma}'} C(\boldsymbol{\sigma}') = \frac{1}{k}\sum_{i=1}^{k} \frac{\sigma_i}{\sigma_i'} \quad \text{subject to} \quad \Pr[S(\mathbf{P}) \geq S_{\min}] \geq Y_{\min}, \quad \mathbf{P} \sim \mathcal{N}\left(\mathbf{0}, \text{diag}\left(\boldsymbol{\sigma}'^2\right)\right), \tag{26}$$

with S_min = 0.80, Y_min = 0.90 and $\sigma_i' = g \cdot w_i \cdot \sigma_i$ (Section 2.9), evaluating S(P) after the optimal refocus when a compensator is used, and validating the result on an independent Monte Carlo sample.

3. Results

3.1. Surface Error Distribution

The deterministic reference configuration of Sections 3.2 and 3.3 superimposes the nominal Zernike departure, MSF ripple, HSF roughness, and alignment errors on the base sphere, giving a non-rotationally symmetric (freeform) surface deviation.

Figure 2 shows the sag of the perturbed surface. At the millimetre scale of the total sag, the surface is indistinguishable from the base sphere, because the manufacturing and alignment errors are of the order of 100 nm to 1 µm. The error is therefore analyzed separately: its individual components (low-order form error, mid-spatial-frequency ripple, high-spatial-frequency roughness, and the alignment-induced deviation from tilt and axial positioning error) are shown in Figure 3, and their superposition in Figure 4. The total

surface error has an RMS value of 501.911 nm and a peak-to-valley value of 2199.577 nm, which correspond, via Equation (5), to an RMS wavefront error of 250.956 nm (0.456λ at 550 nm), as analyzed in Section 3.2.

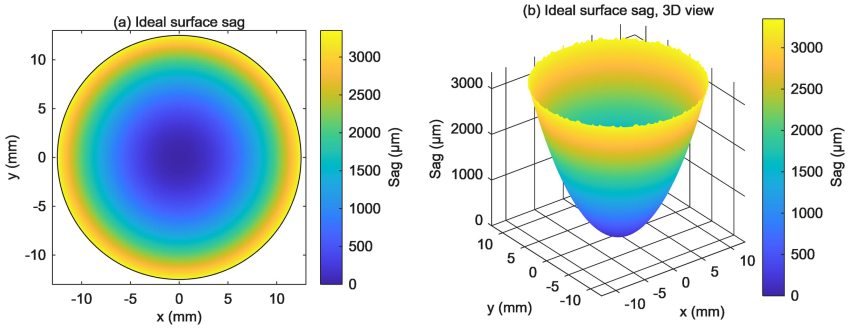

Figure 2. Surface sag of the perturbed surface (base sphere with all manufacturing and alignment errors superimpose): (**a**) two-dimensional map; (**b**) three-dimensional view. At this scale, the sag is dominated by the base sphere; the superimposed surface error is about four orders of magnitude smaller and is shown separately in Figures 3 and 4.

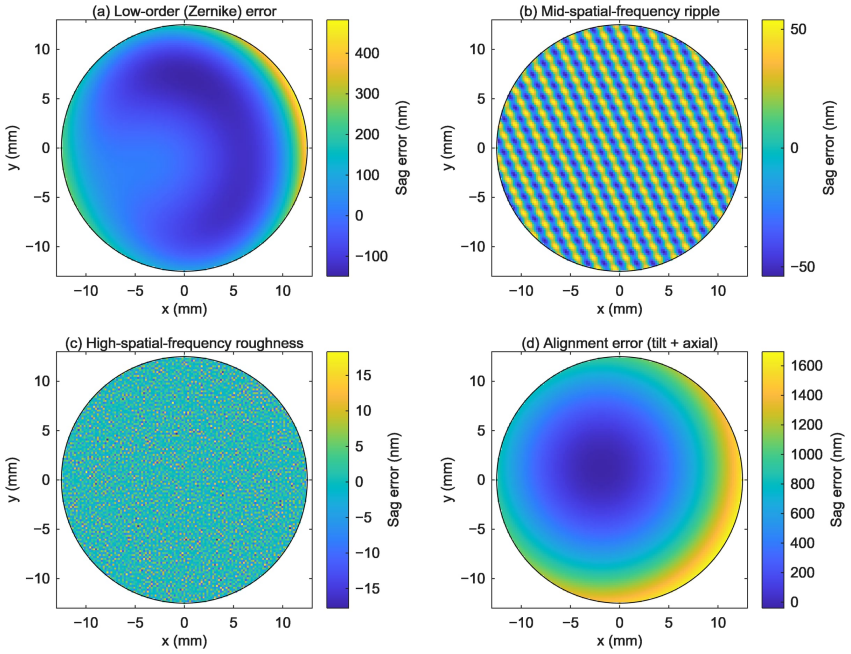

Figure 3. Surface perturbations applied to the base sphere (**a**) low-order form error, (**b**) mid-spatial-frequency (MSF) ripple, (**c**) high-spatial-frequency surface roughness, and (**d**) alignment-induced surface error resulting from tilt and axial positioning error.

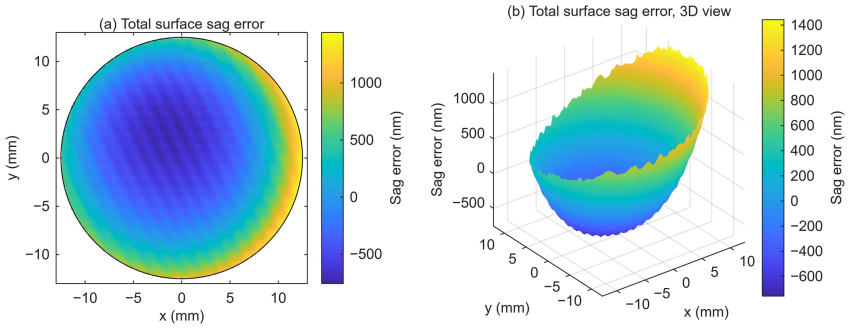

Figure 4. (**a**) Two-dimensional distribution of the combined surface deviation obtained by superimposing the manufacturing and alignment error components. (**b**) Combined deviation, 3D profile.

Figure 3 shows the individual error components and Figure 4 their superposition; the low-order error varies slowly across the aperture, the MSF ripple adds periodic structure, and the HSF roughness adds small-scale random structure.

3.2. Wavefront and Point Spread Function (PSF)

The piston-removed RMS wavefront error of the deterministic configuration is 250.956 nm (0.456λ at 550 nm), far above the λ/14 diffraction-limited criterion, so the perturbed system is not diffraction-limited. At this aberration level, the Maréchal approximation is no longer valid, and the Strehl ratio is therefore computed directly from the PSF (Equation (10)).

Figure 5 compares the PSFs of the nominal and perturbed surfaces. The combined errors broaden the PSF and redistribute energy from the central peak into the surrounding field, as shown by the reduced central intensity and increased side structure in the logarithmic cross-section (Figure 5c). Normalized to the diffraction-limited peak, the perturbed system has a Strehl ratio of 0.0495, far below the diffraction-limited criterion of 0.80 (Table 5).

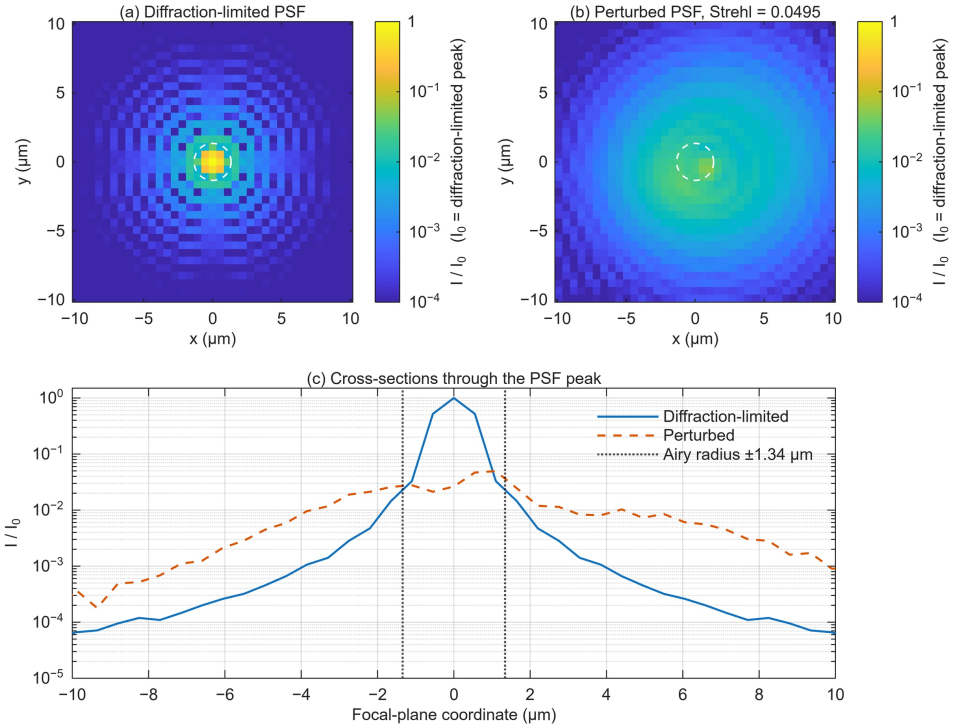

Figure 5. Point spread functions of (**a**) the diffraction-limited system and (**b**) the perturbed system with all errors combined, shown over ±10 μm on a logarithmic scale of normalized intensity I/I_0, where I_0 is the diffraction-limited peak, so that the maximum of (**b**) equals the Strehl ratio (0.0495). Both panels share the same color scale (10^{-4}–1). The dashed circle marks the Airy radius (1.34 μm). (**c**) Cross-sections through the peak of each PSF on a logarithmic scale; the dotted lines mark the Airy radius. Modulation Transfer Function (MTF).

Table 5. Summary of the calculated optical performance metrics for the simulated freeform optical system after introducing manufacturing and alignment errors.

Performance Measure	Value
wavelength	550 nm
RMS WFE	250.956 nm
RMS WFE in waves	0.456 waves
Direct PSF Strehl	0.0495

Figure 6 compares the MTF of the nominal and perturbed systems. The perturbed MTF drops rapidly at low spatial frequencies, consistent with the broadened PSF and reduced Strehl ratio in Figure 5. The two-dimensional MTF (Supplementary Figure S1, with the 909 cycles/mm cutoff marked) additionally shows secondary lobes arising from the MSF ripple and the random roughness and alignment errors.

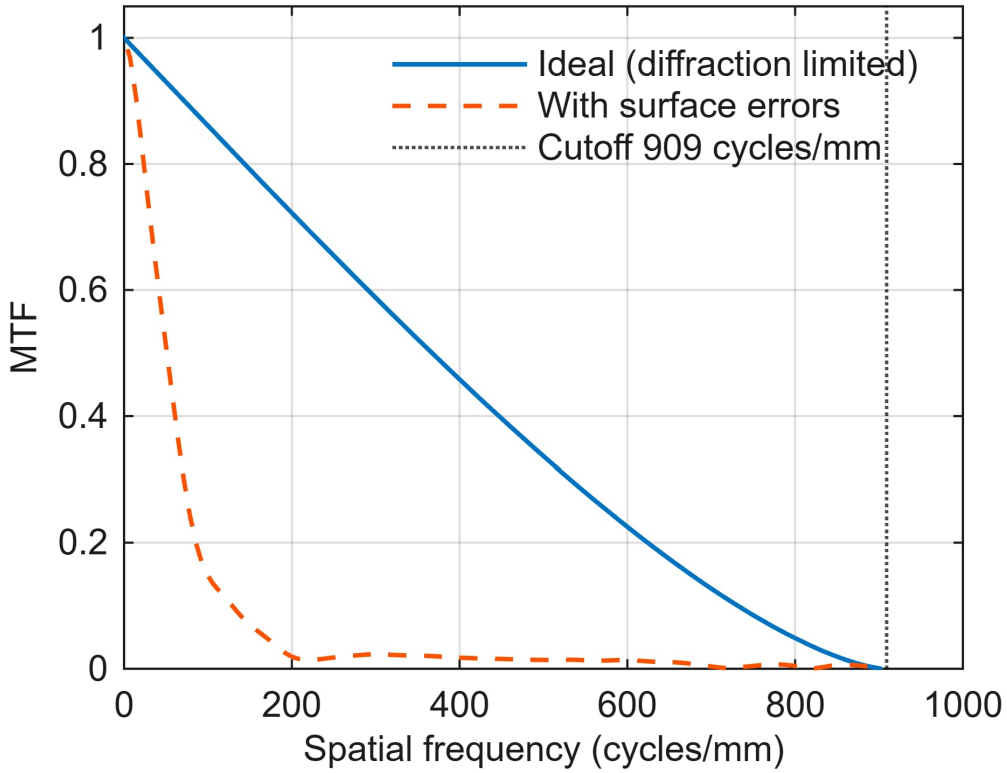

Figure 6. MTF of the nominal and perturbed systems versus spatial frequency; the errors reduce the contrast over most of the frequency range up to the cutoff (909 cycles/mm).

3.3. Monte Carlo Tolerance Analysis

The RMS wavefront error distribution (Figure 7a) is positively skewed: most realizations lie at low-to-intermediate values, but unfavorable combinations of errors produce a long tail toward much larger aberrations. We checked Monte Carlo convergence using the running mean and bootstrap confidence intervals (2000 resamples) for the 5th and 95th percentiles; within ±3.7%, realizations changed the mean RMS wavefront error by 3.4% and the 95th-percentile Strehl ratio by less than 0.6%, so 500 realizations are sufficient. Therefore, five hundred realizations are sufficient for the percentiles reported in Table 6. The direct Strehl ratio (Figure 7b) is strongly right-skewed: most realizations have low values, with a long tail toward unity, so the performance depends strongly on the particular error combination and must be characterized statistically.

Table 6. Summary of the Monte Carlo tolerance analysis, showing the statistical characteristics of the RMS wavefront error (WFE) and direct Strehl ratio over 500 independent realizations.

Metric	Mean	Standard Deviation	95% CI of the Mean	5th Percentile	95th Percentile
RMS WFE	197.955 nm	100.007	[189.189, 206.721]	71.931	383.458
Direct Strehl	0.26222	0.25517	[0.23986, 0.28459]	0.01180	0.74167

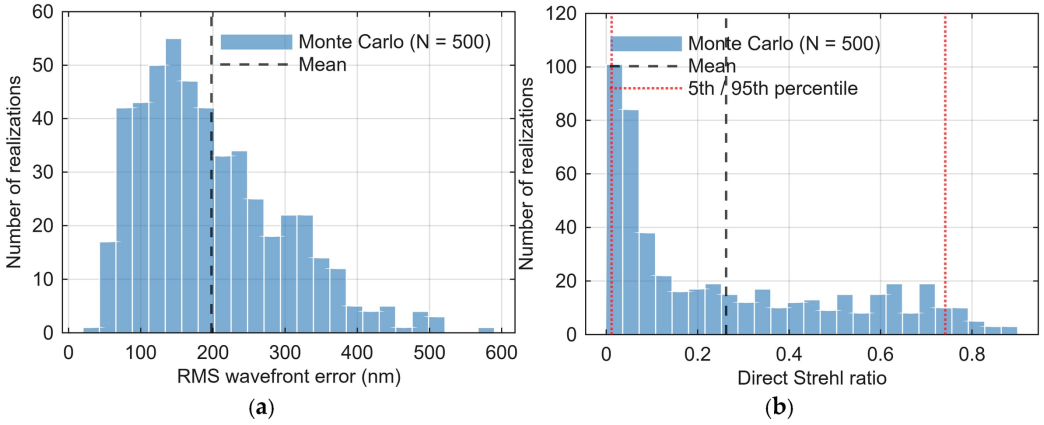

Figure 7. Monte Carlo results for 500 realizations: (**a**) distribution of the RMS wavefront error; (**b**) distribution of the direct Strehl ratio. Statistics are summarized in Table 6; the Strehl ratio of each realization versus its RMS wavefront error is shown in Supplementary Figure S2.

3.4. Numerical Verification

Figure 8a and Supplementary Table S1 compare the computed Strehl ratio of pure defocus with the analytic solution. The Fourier-optics implementation agrees with the analytic value within 0.002–0.14% for $W_{020}/\lambda = 0.05$–0.40, whereas the Maréchal approximation deviates by up to 3.3% at $W_{020}/\lambda = 0.40$. With the tip/tilt-removed wavefront, an additional two-fold zero padding changed the Strehl ratio by 1.5×10^{-3} on average (maximum 9.9×10^{-3}), confirming that the 256 × 256 grid with a window of twice the aperture diameter is sufficient. With the tilt retained, the same test changed the Strehl ratio by up to 0.091 (Figure 8b), and a pure tilt of 90 µrad, which should leave the Strehl ratio at unity, gave 0.995. With the tilt removed, the Strehl ratio for this test is 1.000, and the computed image displacement (2.250 µm) equals the analytic value $f \cdot (n - 1) \cdot \tan\theta$. These results justify the treatment of tilt described in Section 2.4.

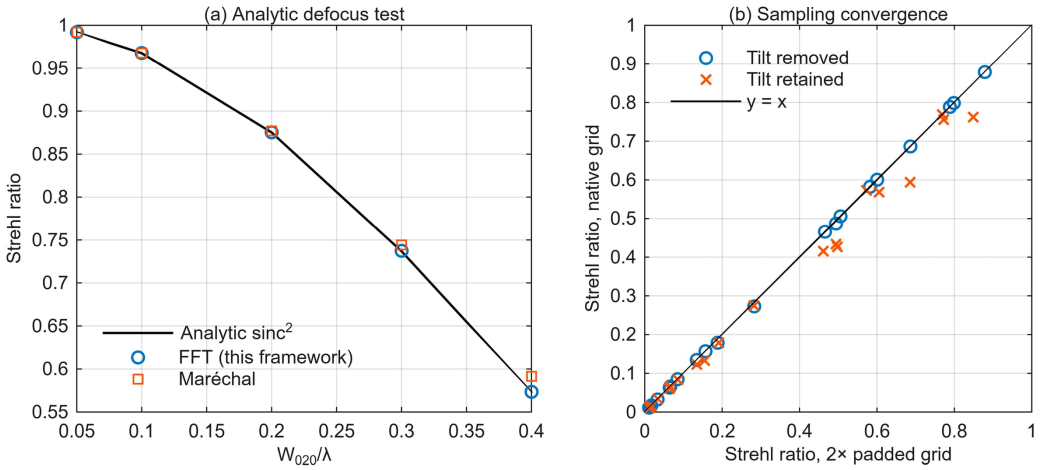

Figure 8. (**a**) Strehl ratio of pure defocus: analytic solution, Fourier-optics computation and Maréchal approximation. (**b**) Strehl ratio computed on the native grid versus a two-fold zero-padded grid, with tip/tilt removed (circles) and retained (crosses); the solid line is y = x.

3.5. Monte Carlo Analysis with a Focus Compensator

With the Strehl ratio computed from the tip/tilt-removed wavefront, the 500-realization Monte Carlo analysis gives a mean Strehl ratio of 0.303 (95% CI 0.278–0.328; 5th–95th percentile 0.014–0.824) and a mean image displacement of 0.78 µm (95th percentile 1.52 µm,

slightly larger than the Airy radius of 1.34 µm; 90.8% of the parts remain within the Airy radius). Only 7.6% of the realizations reach Strehl ≥ 0.80.

When a focus compensator is allowed, the residual RMS wavefront error falls to 41.4 nm, and the mean Strehl ratio rises to 0.790 (95% CI 0.779–0.800; 5th–95th percentile 0.561–0.938). The fraction of acceptable parts rises to 53.4%. The required refocus is 14.6 µm on average and 37.3 µm at the 95th percentile, which defines the adjustment range that the mechanical design must provide.

3.6. Non-Additivity of the Combined Errors

Each error group was evaluated alone for 200 Monte Carlo realizations and compared with the combined model (Table 7, Figure 9).

Table 7. Mean Strehl ratio and RMS wavefront error of each error group acting alone and of all errors combined (200 realizations).

Error Group Acting Alone	Mean Strehl Ratio	Mean RMS WFE (nm)
Axial positioning	0.385	125.3
Low-order form error	0.672	54.9
MSF ripple	0.972	11.8
HSF roughness	0.999	2.4
Tilt (image displacement only)	1.000	98.8
All errors combined	0.298	184.3

A multiplicative prediction ΠS_i misses the combined Strehl ratio by 42% on average (90th percentile 84%), and an additive prediction $1 - \Sigma(1 - S_i)$ by 69%. Even the RMS wavefront error deviates from quadrature addition by 12% on average. The reason is that the surface defocus term and the axial positioning error produce the same r^2 wavefront: their contributions add in amplitude and can reinforce or cancel each other, instead of adding in quadrature. The performance of the system therefore cannot be predicted from separately evaluated error sources.

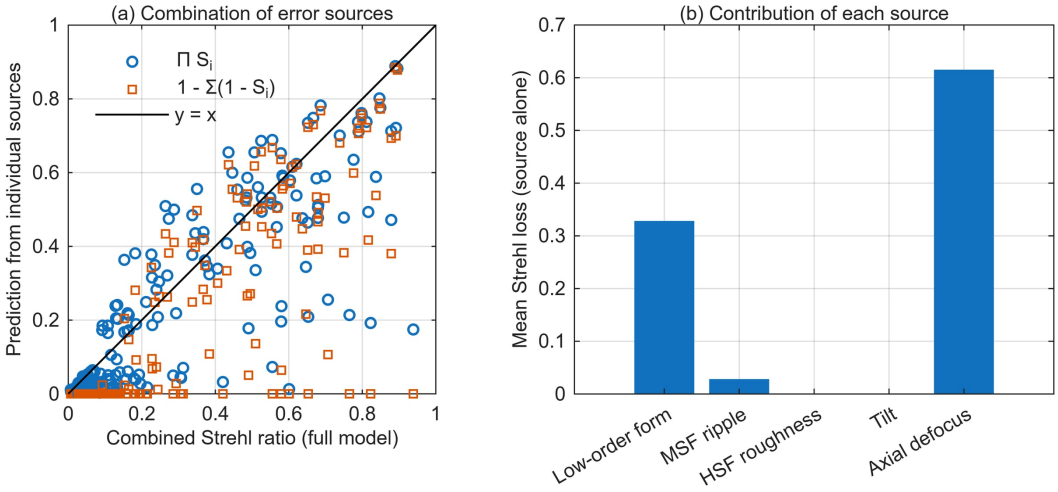

Figure 9. (**a**) Strehl ratio predicted from the individually evaluated error groups (multiplicative ΠS_i and additive $1 - \Sigma(1 - S_i)$) versus the Strehl ratio of the combined model; the solid line is y = x. (**b**) Mean Strehl-ratio loss caused by each error group acting alone.

3.7. Monte Carlo Versus the RSS Estimate

The RSS estimate agrees with the Monte Carlo quadratic mean of the RMS wavefront error to within 0.6–7.5% for the two independent ensembles, a difference of the order of the sampling variation between ensembles, because the wavefront variance adds for independent errors. It fails for the Strehl ratio, underestimating the Monte Carlo mean

by 97% (Table 8, Figure 10), and a linear sum of the one-at-a-time losses even gives a negative value.

Table 8. Comparison of the conventional RSS estimate (Equation (25)) with the Monte Carlo statistics.

Metric	RSS Est.	MC Mean *	MC Median	RSS Err%
Strehl (RSS)	0.0094	0.303	0.175	−96.88
Strehl (linear sum)	−0.396	0.303	0.175	−230.66
RMS WFE [nm]	220.54	205.07	171.75	+7.54
RMS WFE tilt-removed [nm]	189.62	172.33	119.24	+10.04

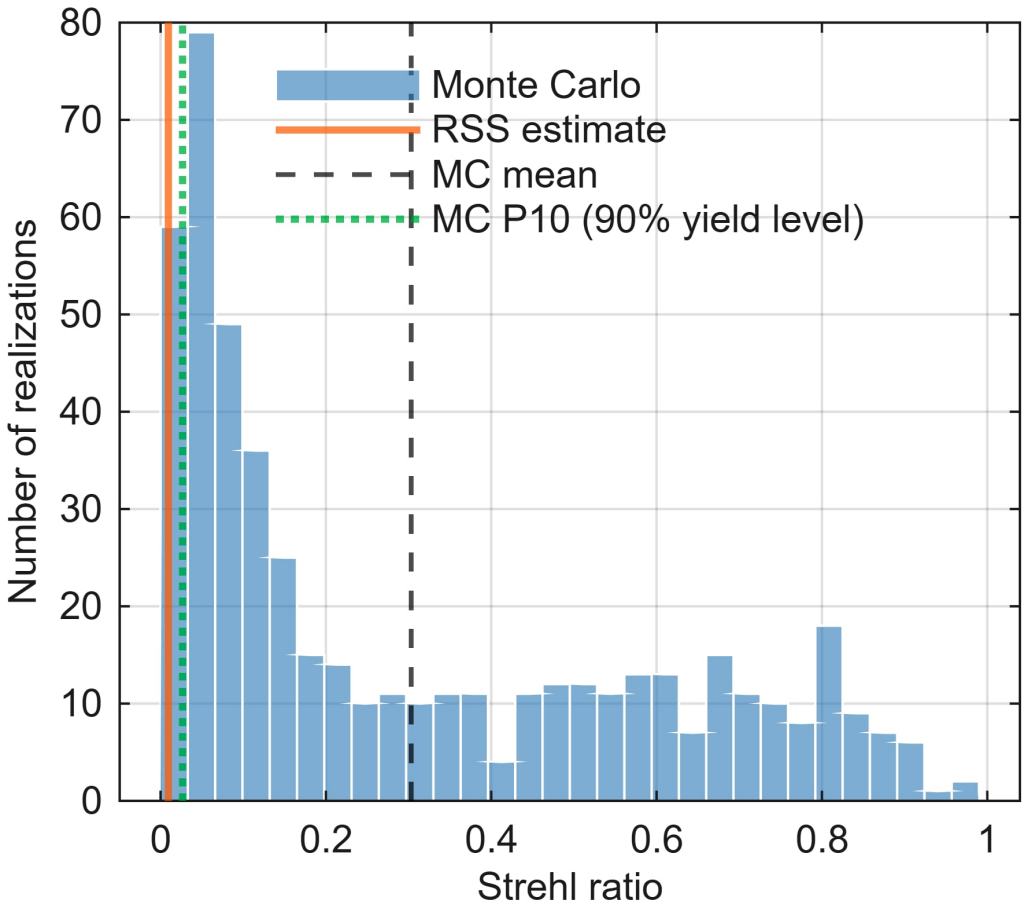

Figure 10. Distribution of the Monte Carlo Strehl ratio (500 realizations) with the RSS estimate, the Monte Carlo mean, and the 10th percentile (level reached by 90% of parts).

3.8. Yield-Based Tolerance Allocation

With the original tolerances, only 7.6% of the parts reach Strehl ≥ 0.80, so the tolerances must be tightened. Table 9 compares three allocation strategies that meet the target of Strehl ≥ 0.80 for 90% of the parts (validated yield 90.5–88.8% on 1000 independent realizations; sampling uncertainty ±1%).

The Strehl-based budget reduces the tolerance cost by 64% relative to uniform tightening and by 27% relative to the RMS-based budget. It relaxes the tilt tolerance because tilt only displaces the image (90th-percentile displacement 1.15 µm, below the Airy radius), and concentrates the budget on axial positioning ($\sigma \approx 2$ µm). The RMS-based budget over-tightens tilt because tilt dominates the RMS wavefront error without affecting the Strehl ratio (Figure 11).

Table 9. Tolerance allocations that meet Strehl ≥ 0.80 for 90% of the parts. Cost index = mean(σ_original/σ_allocated).

Strategy	Cost Index	Axial σ (μm)	Low-Order σ (nm)	Tilt σ x/y (μrad)	Validated Yield
Uniform tightening	7.49	2.7	2.7–10.7	4.0/2.7	90.5%
RMS-based budget	3.67	1.5	12.0–26.6	4.2/4.2	88.8%
Strehl-based budget	2.69	2.0	16.8–18.2	25.1/16.8	90.4%

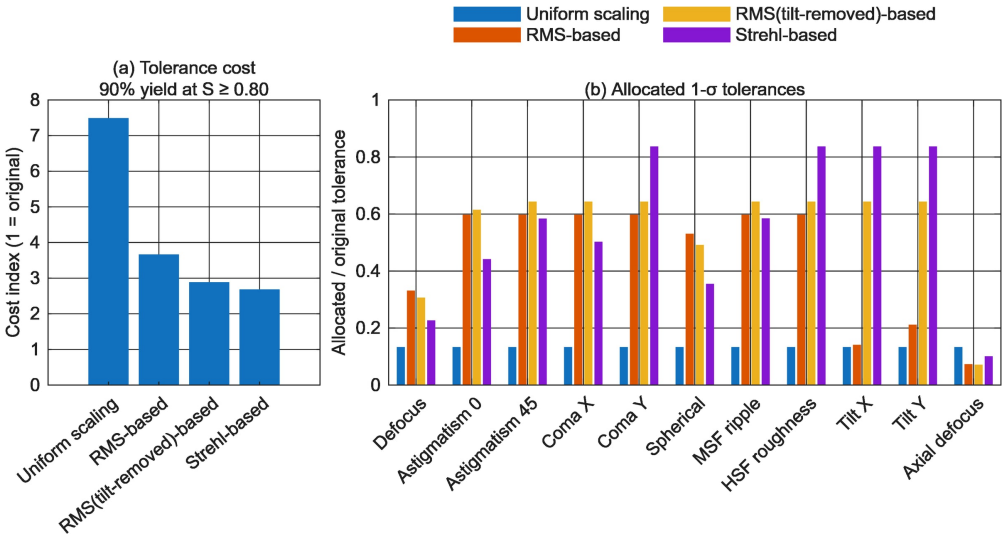

Figure 11. (**a**) Tolerance cost index required by each allocation strategy to reach Strehl ≥ 0.80 for 90% of the parts. (**b**) Ratio of the allocated to the original one-sigma tolerance for each parameter.

3.9. Global Sensitivity Analysis

Table 10 and Figure 12 summarize the total-effect Sobol indices of the Strehl ratio and the RMS wavefront error.

Table 10. Total-effect Sobol indices S_t of the Strehl ratio and of the RMS wavefront error (N = 1000; 95% bootstrap confidence intervals in parentheses).

Parameter	Strehl Ratio	RMS WFE (Tilt Retained)	RMS WFE (Tip/Tilt Removed)
Axial positioning	1.01 (0.93–1.09)	0.86	0.99
Surface defocus	0.27 (0.24–0.31)	0.088	0.11
Spherical aberration	0.020	0.001	0.002
Coma X	0.005	<0.001	<0.001
Coma Y	0.001	<0.001	<0.001
Astigmatism 0°	0.009	<0.001	<0.001
Astigmatism 45°	0.004	<0.001	<0.001
MSF ripple	0.003	<0.001	<0.001
HSF roughness	<0.001	<0.001	<0.001
Tilt X	<0.001	0.110	<0.001
Tilt Y	<0.001	0.027	<0.001

Tilt contributes to the RMS wavefront error only when the tilt is retained (S_t = 0.110 and 0.027); once the best-fit tip/tilt is removed, its indices vanish, as for the Strehl ratio, because a rigid-body tilt only displaces the image (Table 10; Figure 12b). For comparison, a standardized linear regression of the same Monte Carlo data explains only 2.4% of the Strehl-ratio variance (R^2 = 0.024) and misranks the parameters, which confirms that a global variance-based method is required.

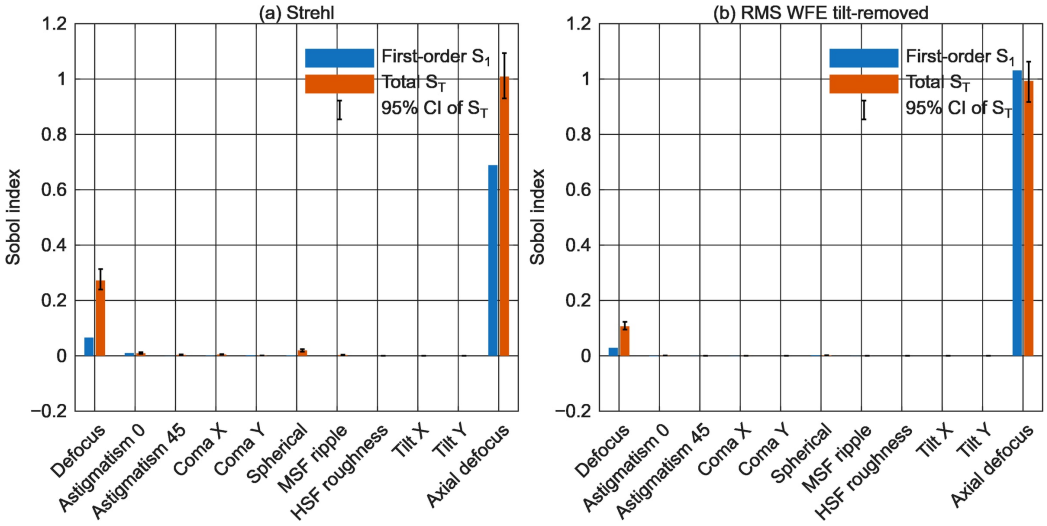

Figure 12. First-order (S_1) and total-effect (S_t) Sobol indices of (**a**) the Strehl ratio and (**b**) the tip/tilt-removed RMS wavefront error. Error bars show the 95% bootstrap confidence intervals of S_t.

4. Discussion

4.1. Error Sources and Implications for Tolerancing

The error sources contribute very unequally. For this F/2 system, the Strehl ratio is governed by focus: axial positioning and surface defocus explain almost all of the variance (Table 10) and interfere because they act on the same wavefront mode (Section 3.7). The remaining low-order terms have a secondary effect. MSF ripple and HSF roughness affect mainly the MTF at mid and high spatial frequencies and the scattered light, and tilt only displaces the image, so it matters for line-of-sight accuracy rather than for image sharpness.

Through the workflow of Section 2.10, these findings lead to three design decisions. First, axial position and surface defocus must be toleranced together, and the Strehl ratio cannot be budgeted with linear RSS methods, which are reliable only for the RMS wavefront error (Section 3.8). Second, because one alignment degree of freedom dominates, a focus compensator is the most effective measure: a refocus range of about ± 40 µm raises the mean Strehl ratio from 0.30 to 0.79 and the yield from 7.6% to 53.4%. Third, if no compensator can be used, the Strehl-based allocation reaches the 90% yield target at 64% and 27% lower cost than uniform tightening and the RMS-based budget, respectively, mainly by relaxing the tilt tolerance, which an RMS-based ranking over-weights. A fourth, system-level option follows from $W_{020} = \delta z/(8N^2)$: slowing the system from F/2 to F/4 reduces the axial-focus sensitivity by a factor of four.

4.2. Comparison with Previous Studies

Unlike previous studies that address one error class at a time, such as local surface tolerances [6,8], surface-frequency bands [7] or image-quality-based tolerancing [9], the present framework evaluates all error classes together. The results show why this is necessary: the dominant error sources interact, so separately derived tolerances and linear budgets misjudge the resulting Strehl ratio, which only a statistical, yield-based treatment captures.

4.3. Applicability, Limitations and Future Work

The framework requires only the wavelength, the aperture and F-number, the nominal surface sag (as a Zernike expansion or a sampled sag map) and the statistical tolerances of each error source. It can therefore be applied directly to any single freeform or aspheric surface evaluated at one field point, and to a multi-element system if the wavefront contribution of the toleranced surface is added to the system pupil function. The numerical results,

however, are specific to the F/2 singlet studied here. The dominance of axial focus scales with the F-number through $W_{020} = \delta z/(8N^2)$ (Section 2.5.2); for an F/8 system the same axial error produces a 16 times smaller wavefront error, and the ranking of the error sources may change. The present implementation has several limitations. It is monochromatic and on-axis, uses scalar Fourier optics and a thin-lens approximation, and does not include polarization, chromatic dispersion, or thermal deformation. The error sources were assumed to be statistically independent, whereas practical fabrication processes may correlate them, and the tolerance values in Table 4 are representative assumptions rather than measured process data. Finally, the predictions have not yet been validated experimentally.

Future work will address these limitations by extending the framework to broadband and off-axis fields, coupling it to ray tracing for thick-lens and multi-surface systems, including correlated error sources taken from metrology data, and validating the predictions on manufactured freeform components. In addition, the sensitivity metrics derived here (total Sobol indices and yield) will be used directly as merit-function terms in the optimization of the nominal freeform surface, so that desensitized freeform designs can be obtained.

5. Conclusions

A general computational framework for the tolerance and sensitivity analysis of freeform optical surfaces has been presented. It applies low-order form error, mid-spatial-frequency ripple, high-spatial-frequency roughness, tilt and axial positioning error simultaneously to one surface, propagates them to the PSF, MTF, RMS wavefront error and Strehl ratio, and combines Monte Carlo statistics, Sobol sensitivity analysis and yield-based tolerance allocation. The F/2 singlet demonstration leads to three general conclusions. First, error sources acting on the same wavefront mode, here axial position and surface defocus, interact, so their combined effect cannot be predicted from separately evaluated errors. Second, linear RSS budgets are adequate for the RMS wavefront error but not for the Strehl ratio, which must be tolerance statistically. Third, global sensitivity indices identify the dominant errors and the need for a compensator: a focus compensator raised the mean Strehl ratio from 0.30 to 0.79, and a Strehl-based allocation met the yield target at 64% lower tolerance cost than uniform tightening. Extension to broadband, off-axis, and multi-element systems and experimental validation are left for future work.

Supplementary Materials: The following supporting information can be downloaded at: https://www.mdpi.com/article/10.3390/photonics13121130/s1, Figure S1: Two-dimensional MTF of the diffraction-limited and perturbed systems; Figure S2: Direct Strehl ratio versus RMS wavefront error for the 500 Monte Carlo realizations; Table S1: Verification of the Fourier-optics implementation against the analytic Strehl ratio of pure defocus.

Author Contributions: Conceptualization, R.A.S.; methodology, R.A.S. and N.A.; software, R.A.S.; validation, N.A. and A.A.-M.; formal analysis, R.A.S.; writing—original draft preparation, R.A.S.; writing—review and editing, A.A.-M. and G.H.A.; supervision, A.A.-M. All authors have read and agreed to the published version of the manuscript.

Funding: This research was funded by the Ongoing Research Funding Program (ORF-2026-1672), King Saud University, Riyadh, Saudi Arabia.

Data Availability Statement: The MATLAB code and data supporting the findings of this study are available from the corresponding author upon reasonable request.

Acknowledgments: The authors appreciate the valuable discussions and technical comments provided by colleagues during the preparation of this work. During the preparation of this manuscript, the authors used PaperPal to assist with language editing and grammatical refinement. The authors have reviewed and edited the output and take full responsibility for the content of this publication.

Conflicts of Interest: The authors declare no conflict of interest.

Abbreviations

The following abbreviations are used in this manuscript:

OPD	Optical Path Difference
FFT	Fast Fourier Transform
MTF	Modulation Transfer Function
MSF	Mid-Spatial Frequency
OTF	Optical Transfer Function
PSF	Point Spread Function
RMS	Root Mean Square
RSS	Root-Sum-Square.
HSF	High-Spatial Frequency
CI	Confidence Interval
WFE	Wavefront Error

References

1. Thompson, K.P.; Rolland, J.P. Freeform optical surfaces: A revolution in imaging optical design. *Opt. Photonics News* **2012**, *23*, 30–35. [CrossRef]
2. Gross, H. (Ed.) *Handbook of Optical Systems, Volume 1: Fundamentals of Technical Optics*; Wiley-VCH: Weinheim, Germany, 2005. [CrossRef]
3. Malacara, D. (Ed.) *Optical Shop Testing*, 3rd ed.; John Wiley & Sons: Hoboken, NJ, USA, 2007.
4. Goodman, J.W. *Introduction to Fourier Optics*, 4th ed.; W. H. Freeman: New York, NY, USA, 2017.
5. Youngworth, R.R.; Stone, B.D. Simple estimates for the effects of mid-spatial-frequency surface errors on image quality. *Appl. Opt.* **2000**, *39*, 2198–2209. [CrossRef] [PubMed]
6. Deng, Y.; Tan, Y.; Wu, X.; Zhu, J. Local tolerance and quality evaluation for optical surfaces. *Optica* **2022**, *9*, 1039–1049. [CrossRef]
7. Fan, R.; Wei, S.; Ji, H.; Qian, Z.; Tan, H.; Mo, Y.; Ma, D. Surface variation analysis of freeform optical systems over surface frequency bands for prescribed wavefront errors. *Opt. Laser Technol.* **2024**, *178*, 111223. [CrossRef]
8. Fan, R.; Wei, S.; Qian, Z.; Ji, H.; Tan, H.; Mo, Y.; Yang, L.; Ma, D. Iterative critical ray tracing for local tolerance analysis of freeform imaging systems. *Opt. Commun.* **2025**, *575*, 131299. [CrossRef]
9. Chen, J.; Mao, B.; Cai, P.; Zhang, C.; Wu, R.; Han, B.; Gao, A. Image quality evaluation and tolerance analysis method for optical-digital imaging systems. *Opt. Express* **2026**, *34*, 5885–5902. [CrossRef] [PubMed]
10. Duan, Y.; Zhang, X. Freeform optics characterization with surface registration and fitting algorithms for optical point-based spatial path 3D topography metrology. *Appl. Opt.* **2023**, *62*, 573–583. [CrossRef] [PubMed]
11. Wang, M.; Zhong, W.; Zeng, W.; Gao, F.; Yu, Y.; Scott, P.; Jiang, X. Towards high-speed on-machine measurement of freeform surfaces: A dynamic error calibration method. *Light Adv. Manuf.* **2025**, *6*, 831–842. [CrossRef]
12. Greivenkamp, J.E. *Field Guide to Geometrical Optics*; SPIE Press: Bellingham, WA, USA, 2004.
13. Forbes, G.W. Characterizing the shape of freeform optics. *Opt. Express* **2012**, *20*, 2483–2499. [CrossRef] [PubMed]
14. Ye, J.; Chen, L.; Li, X.; Yuan, Q.; Gao, Z. Review of optical freeform surface representation technique and its application. *Opt. Eng.* **2017**, *56*, 110901. [CrossRef]
15. Mahajan, V.N. *Aberration Theory Made Simple*, 2nd ed.; SPIE Press: Bellingham, WA, USA, 2011. [CrossRef]
16. Saltelli, A.; Annoni, P.; Azzini, I.; Campolongo, F.; Ratto, M.; Tarantola, S. Variance-based sensitivity analysis of model output. Design and estimator for the total sensitivity index. *Comput. Phys. Commun.* **2010**, *181*, 259–270. [CrossRef]
17. Jansen, M.J.W. Analysis of variance designs for model output. *Comput. Phys. Commun.* **1999**, *117*, 35–43. [CrossRef]

Disclaimer/Publisher's Note: The statements, opinions and data contained in all publications are solely those of the individual author(s) and contributor(s) and not of MDPI and/or the editor(s). MDPI and/or the editor(s) disclaim responsibility for any injury to people or property resulting from any ideas, methods, instructions or products referred to in the content.